Lehmann, J., Schulmann, K., Lexa, O., Závada, P., Štípská, P., Hasalová, P., Belyanin, G., and Corsini, M., 2017, Detachment folding of partially molten crust in accretionary orogens: A new magma-enhanced vertical mass and heat transfer mechanism: Lithosphere, doi:10.1130/L670.1.

GSA Data Repository Item 2017331

APPENDIX A: ANALYTICAL METHODS FOR $^{40}Ar/^{39}Ar$ AGE DETERMINATION

Mineral separates of white mica, biotite and hornblende were obtained after crushing and handpicking of single grains under a binocular microscope. The minerals were repeatedly cleaned ultrasonically in distilled water and subsequently wrapped in aluminum foils.

The crystals analyzed at Geoazur laboratory (University of Nice Sophia Antipolis) from samples *M680A*, *M717A* and *M635B* were co-irradiated for 30 h in the nuclear reactor at McMaster University in Hamilton (Canada) in position 5c, along with Hb3gr hornblende monitor (1073.6 ± 5.4 Ma, Jourdan et al., 2006). The total neutron flux density during irradiation was 8.8E18 neutron cm^{-2} with a maximum flux gradient estimated at 0.2 % in the volume where the samples were included. Back in Nice, single grains of amphibole and biotite were heated with a CO_2 Synrad laser, and the extracted gas was purified in a stainless and glass extraction line using two Al–Zr getters (working at 400 °C and ambient temperature respectively) and a liquid nitrogen cold trap. Isotopic measurements were performed with a VG3600 mass spectrometer and a Daly-photomultiplier system. Blank measurements were obtained before and after every three sample run. The correction factors for interfering isotopes correspond to $(^{39}Ar/^{37}Ar)Ca = (7.30 \pm 0.28) \times 10^4$; $(^{36}Ar/^{37}Ar)Ca = (2.82 \pm 0.03) \times 10^4$ and $(^{40}Ar/^{39}Ar)K = (2.97 \pm 0.06) \times 10^2$. Mass discrimination values range from 1.00474 to 1.00738 ± 1 % (1σ) per dalton (atomic mass unit).

The three samples *M776B* (biotites), *M776B-1* and *M776B-2* (white micas) analyzed at SPECTRUM (University of Johannesburg), were vacuum sealed in a ca. 15 cm-long silica glass tube with a 1 cm outer diameter along with other samples and monitors and then irradiated at the NTP radioisotopes SAFARI1 nuclear reactor at Pelindaba, South

Africa, for 20 hours in position B2W with the reactor running at 20 MW. Two 0.2 mg aliquots of each sample were analyzed by stepwise heating, using a defocused beam from a continuous Nd-YAG 1064 nm laser and a MAP 215-50 noble gas mass spectrometer. Signals were measured on a Johnston focused-flow electron multiplier providing excellent linearity in analogue mode. The Fish Canyon sanidine (28.31 ± 0.04 Ma) and Hb3gr amphibole (1080.40 ± 1.10 Ma) (Renne et al., 2010), as well as McClure Mountain amphibole (523.00 ± 1.00 Ma) (Schoene and Bowring, 2006) standards, were used as monitors, yielding within uncertainty limits, identical J-values. A slight flux gradient was monitored and taken into account by placing standards at the bottom and top of the irradiation package. The value for the ^{40}K decay constant derived by Renne et al. (2010) was utilized. Measurement control and data reduction was carried out using an in-house software suite that includes full error propagation by Monte Carlo procedures. Uncertainties are shown at the 95 % (2σ) confidence level.

The criteria for defining plateau ages were as follows: (i) a plateau age should contain at least 70 % of the total released ^{39}Ar, (ii) there should be at least three successive steps in the plateau, and (iii) the integrated age of the plateau should agree with each apparent age of the plateau within a 2σ error confidence interval.

TABLE 1A: SUMMARY OF $^{40}Ar/^{39}Ar$ GEOCHRONOLOGY DATA FROM GEOAZUR LABORATORY (UNIVERSITY OF NICE - SOPHIA-ANTIPOLIS)

Step number	Temp [°C]	$^{40}Ar/^{39}Ar$	±	1σ	$^{37}Ar/^{39}Ar$	±	1σ	$^{36}Ar/^{39}Ar$	±	1σ	Ca/K	$^{40}Ar^*$ (%)	$^{39}Ar_K$ (%)	$^{40}Ar^*/^{39}Ar_K$	±	1σ	Age (Ma)	±	2σ	Included
White mica M680A (experiment k468) [45.23187°N, 97.98959°E]																				
J = 0.0195358 ± 0.0000977																				
K468-1	381	-23.90	±	60.73	-248.94	±	776.72	0.73	±	3.03		1091.30	0.00	-220.72	±	766.39	0.00	±	16349.88	no
K468-2	451	10.55	±	0.13	0.45	±	0.44	0.00	±	0.00		98.99	3.52	10.45	±	0.77	335.85	±	45.22	yes
K468-3	476	10.89	±	0.11	-0.07	±	0.04	0.00	±	0.00		100.30	35.12	10.92	±	0.14	349.79	±	7.91	yes
K468-4	485	10.58	±	0.11	-0.18	±	0.09	0.00	±	0.00		103.18	14.13	10.91	±	0.18	349.52	±	10.67	yes
K468-5	502	10.22	±	0.13	-0.41	±	0.24	0.00	±	0.00		107.77	4.70	11.01	±	0.43	352.43	±	24.93	yes
K468-6	525	10.43	±	0.11	-0.39	±	0.10	0.00	±	0.00		105.67	11.00	11.02	±	0.29	352.57	±	16.87	yes
K468-7	585	10.53	±	0.11	-0.07	±	0.05	0.00	±	0.00		101.08	20.37	10.65	±	0.16	341.74	±	9.20	yes
K468-8	655	10.72	±	0.11	-0.15	±	0.18	0.00	±	0.00		98.06	5.94	10.51	±	0.27	337.69	±	15.96	yes
K468-9	753	10.90	±	0.15	-0.32	±	0.71	-0.01	±	0.00		122.66	1.82	13.36	±	1.45	419.45	±	81.27	yes
K468-10	Fusion	11.82	±	0.15	-0.70	±	0.28	0.00	±	0.00		103.85	3.39	12.27	±	0.90	388.61	±	51.44	yes
White mica M717A (experiment k470) [45.23685°N, 98.061°E]																				
J = 0.0195349 ± 0.0000977																				
K470-1	613	12.56	±	0.14	0.18	±	0.09	0.00	±	0.00		88.89	3.31	11.17	±	0.29	356.84	±	16.63	yes
K470-2	649	11.02	±	0.11	0.10	±	0.10	0.00	±	0.00		98.95	2.46	10.90	±	0.25	349.15	±	14.75	yes
K470-3	693	10.90	±	0.11	0.05	±	0.01	0.00	±	0.00		100.31	45.39	10.94	±	0.11	350.11	±	6.49	yes
K470-4	715	10.95	±	0.11	0.06	±	0.02	0.00	±	0.00		101.36	15.62	11.10	±	0.12	354.96	±	7.15	yes
K470-5	735	10.91	±	0.11	0.00	±	0.03	0.00	±	0.00		101.18	11.61	11.04	±	0.13	353.08	±	7.65	yes
K470-6	765	10.90	±	0.11	0.02	±	0.02	0.00	±	0.00		101.40	10.09	11.05	±	0.13	353.44	±	7.46	yes
K470-7	820	11.02	±	0.12	0.21	±	0.08	0.00	±	0.00		102.35	3.92	11.27	±	0.20	359.94	±	11.40	yes

K470-8	Fusion	11.46	±	0.12	0.13	±	0.03	0.00	±	0.00							99.13	7.33	11.36	±	0.14	362.30	±	8.37	yes
Amphibole M635B (experiment k473) [45.26824°N, 98.1497°E]																									
J = 0.0195259 ± 0.0000976																									
K473-1	825	24.82	±	0.91	1.35	±	1.31	0.03	±	0.01							65.46	0.35	16.23	±	2.91	497.84	±	156.16	no
K473-2	866	13.08	±	2.71	1.86	±	7.23	0.00	±	0.07							108.81	0.09	14.21	±	19.85	442.81	±	1097.22	no
K473-4	1220	11.66	±	0.18	4.95	±	0.32	0.01	±	0.00							86.01	1.86	10.07	±	0.66	324.53	±	39.06	yes
K473-5	1365	11.09	±	0.11	6.31	±	0.21	0.00	±	0.00							99.98	33.72	11.14	±	0.13	355.89	±	7.40	yes
K473-6	Fusion	10.98	±	0.11	5.65	±	0.19	0.00	±	0.00							100.21	63.98	11.05	±	0.12	353.35	±	6.90	yes

TABLE 1B: SUMMARY OF $^{40}Ar/^{39}Ar$ GEOCHRONOLOGY DATA FROM SPECTRUM (UNIVERSITY OF JOHANNESBURG)[a]

Step number	Laser temperature (°C)	$^{40}Ar/^{39}Ar$	±	1σ	$^{37}Ar/^{39}Ar$	±	1σ	$^{36}Ar/^{39}Ar$	±	1σ	Ca/K	±	1σ	Cl/K	±	1σ	$^{40}Ar^*$ (%)	^{39}Ar (%)	$^{40}Ar^*/^{39}Ar$	±	1σ	Age (Ma)	±	2σ	Included
White mica M776B-1 [45.23685°N, 98.061°E]																									
J = 0.008156 ± 0.000012																									
6617_6_1_9.50A	500				-			-			-			-			0.01	-132.92	±	141.70	0.00	±	3069.18	no
6618_6_1_9.65A	565				-			-			-			0.2082	±	0.0726	0.01	74.66	±	66.66	857.04	±	2087.25	no
6619_6_1_9.79A	630				0.1449	±	0.0068				0.2745	±	0.0293	0.0176	±	0.0019	1.54	25.85	±	0.34	344.74	±	8.17	yes
6620_6_1_9.94A	695				0.0144	±	0.0024				0.0272	±	0.0053	0.0062	±	0.0007	2.98	26.35	±	0.23	350.82	±	5.84	yes
6622_6_1_10.08A	760				0.0117	±	0.0015				0.0222	±	0.0035	0.0019	±	0.0002	6.15	26.29	±	0.11	350.06	±	3.12	yes
6623_6_1_10.23A	825				0.0035	±	0.0011				0.0066	±	0.0021	0.0015	±	0.0002	5.77	26.08	±	0.15	347.53	±	3.91	yes
6624_6_1_10.37A	890				0.0021	±	0.0017				0.0041	±	0.0032	0.0016	±	0.0002	5.24	25.81	±	0.51	344.31	±	12.83	yes
6625_6_1_10.52A	955				0.0030	±	0.0006				0.0057	±	0.0013	0.0015	±	0.0002	17.95	25.99	±	0.10	346.46	±	2.89	yes
6627_6_1_10.66A	1020				0.0007	±	0.0003				0.0013	±	0.0007	0.0016	±	0.0002	26.17	25.87	±	0.08	344.98	±	2.49	yes
6628_6_1_10.81A	1085				0.0018	±	0.0014				0.0035	±	0.0027	0.0015	±	0.0002	7.28	25.58	±	0.17	341.41	±	3.92	yes
6629_6_1_10.95A	1150				0.0006	±	0.0005				0.0012	±	0.0009	0.0015	±	0.0002	11.62	25.52	±	0.11	340.79	±	2.93	yes
6630_6_1_11.10A	1215				0.0006	±	0.0006				0.0011	±	0.0012	0.0015	±	0.0002	9.39	25.76	±	0.13	343.61	±	3.53	yes
6632_6_1_11.25A	1280				0.0047	±	0.0018				0.0088	±	0.0035	0.0015	±	0.0002	3.91	25.86	±	0.15	344.92	±	4.01	yes
6633_6_1_11.40A	1345				0.0015	±	0.0095				0.0028	±	0.0180	0.0014	±	0.0003	1.02	25.76	±	0.49	343.64	±	11.95	yes
6634_6_1_11.55A	1400				0.0129	±	0.0081				0.0245	±	0.0155	0.0017	±	0.0003	0.97	25.48	±	0.44	340.20	±	10.79	yes
White mica M776B-2 [45.23685°N, 98.061°E]																									
J = 0.008155 ± 0.000012																									
7632_6_1_776B_9.77A	500				-			-			-			0.0083	±	0.0005	1.50	24.54	±	0.48	328.72	±	11.79	no
7633_6_1_776B_9.95A	560				0.0028	±	0.0037				0.0053	±	0.0070	0.0023	±	0.0001	7.97	25.70	±	0.15	342.94	±	3.71	yes
7634_6_1_776B_10.12A	620				0.0024	±	0.0032				0.0046	±	0.0060	0.0016	±	0.0001	7.96	26.08	±	0.15	347.46	±	3.90	yes
7636_6_1_776B_10.29A	680				0.0031	±	0.0028				0.0059	±	0.0054	0.0018	±	0.0001	7.02	25.63	±	0.16	342.05	±	4.28	yes
7637_6_1_776B_10.47A	740				0.0015	±	0.0022				0.0028	±	0.0042	0.0016	±	0.0001	9.70	26.23	±	0.09	349.33	±	2.69	yes
7638_6_1_776B_10.64A	800				-			-			-			0.0016	±	0.0006	3.04	25.29	±	1.15	337.90	±	28.24	yes
7639_6_1_776B_10.81A	860				-			-			-			0.0023	±	0.0006	4.73	27.32	±	0.61	362.49	±	13.99	yes
7641_6_1_776B_10.99A	920				0.0021	±	0.0022				0.0040	±	0.0041	0.0016	±	0.0001	12.61	26.07	±	0.08	347.34	±	2.49	yes
7642_6_1_776B_11.16A	980				0.0025	±	0.0084				0.0048	±	0.0159	0.0014	±	0.0002	2.82	25.34	±	0.24	338.50	±	5.90	yes
7643_6_1_776B_11.33A	1040				-	±	-				-		-	0.0016	±	0.0001	15.83	26.08	±	0.05	347.51	±	2.03	yes
7644_6_1_776B_11.51A	1100				0.0005	±	0.0031				0.0010	±	0.0058	0.0016	±	0.0001	7.51	25.43	±	0.12	339.56	±	3.30	yes
7646_6_1_776B_11.68A	1160				-		-				-		-	0.0015	±	0.0001	3.33	25.62	±	0.20	341.93	±	5.27	yes
7647_6_1_776B_11.85A	1220				-		-				-		-	0.0014	±	0.0001	4.03	25.91	±	0.18	345.45	±	4.85	yes
7648_6_1_776B_12.03A	1280				-		-				-		-	0.0014	±	0.0001	7.15	26.42	±	0.13	351.62	±	3.60	yes
7649_6_1_776B_12.20A	1340				-		-				-		-	0.0014	±	0.0001	4.05	26.08	±	0.21	347.53	±	5.55	yes
7651_6_1_776B_12.40A	1400				0.1297	±	0.0394				0.2457	±	0.0750	0.0008	±	0.0004	0.76	20.12	±	0.80	273.80	±	20.60	no
Biotite M776B [45.23685°N, 98.061°E]																									
J = 0.008160 ± 0.000012																									
6636_7_1_Bt_9.50A	500				0.0499	±	0.0098				0.0946	±	0.0207	0.0107	±	0.0012	1.45	23.23	±	0.55	312.83	±	14.34	no
6637_7_1_Bt_9.60A	565				0.0179	±	0.0022				0.0340	±	0.0054	0.0080	±	0.0009	7.66	24.57	±	0.15	329.32	±	3.69	yes
6638_7_1_Bt_9.70A	630				0.0024	±	0.0022				0.0045	±	0.0043	0.0073	±	0.0008	7.41	24.74	±	0.17	331.32	±	4.30	yes

6639_7_1_Bt_9.80A	695	0.0015	±	0.0012	0.0028	±	0.0022	0.0073	±	0.0008	11.29	25.00	±	0.10	334.50	±	2.71	yes
6641_7_1_Bt_9.90A	760	-		-	-		-	0.0074	±	0.0008	10.82	25.01	±	0.07	334.66	±	2.39	yes
6642_7_1_Bt_10.00A	825	0.0006	±	0.0011	0.0011	±	0.0020	0.0071	±	0.0008	13.57	24.94	±	0.08	333.76	±	2.39	yes
6643_7_1_Bt_10.10A	890	0.0014	±	0.0015	0.0026	±	0.0028	0.0069	±	0.0008	7.72	24.99	±	0.12	334.48	±	3.25	yes
6644_7_1_Bt_10.20A	955	0.0026	±	0.0018	0.0049	±	0.0034	0.0073	±	0.0008	8.69	25.16	±	0.14	336.46	±	3.98	yes
6646_7_1_Bt_10.30A	1020	-		-	-		-	0.0072	±	0.0008	7.23	25.25	±	0.12	337.58	±	3.34	yes
6647_7_1_Bt_10.40A	1085	-		-	-		-	0.0074	±	0.0008	3.97	25.08	±	0.27	335.56	±	6.83	yes
6648_7_1_Bt_10.50A	1150	-		-	-		-	0.0074	±	0.0008	7.16	24.91	±	0.54	333.49	±	13.85	yes
6649_7_1_Bt_10.70A	1215	-		-	-		-	0.0075	±	0.0008	9.80	25.18	±	0.13	336.74	±	3.44	yes
6651_7_1_Bt_10.90A	1280	-		-	-		-	0.0073	±	0.0009	1.23	24.25	±	0.69	325.36	±	16.70	yes
6652_7_1_Bt_11.10A	1345	-		-	-		-	0.0046	±	0.0010	0.52	18.44	±	1.79	252.65	±	46.12	no
6653_7_1_Bt_11.70A	1400	0.0150	±	0.0126	0.0284	±	0.0240	0.0084	±	0.0012	1.49	23.62	±	0.90	317.62	±	22.41	no

[a]Step temperatures optically estimated.

APPENDIX B: ANALOGUE MODELLING OF CRUSTAL-SCALE DETACHMENT FOLDS

Experimental setup

The analogue modelling apparatus consists of two heating plates confined between two glass panes (1.5 cm thick), a top heat source (several lightbulbs in a row mounted in a steel sheet case), a track of several rotating cylinders over which one of the plates moves laterally between the glass panes and a control unit that allows adjustment of the heating temperature of both plates and the light/heat intensity of the top heat source (Fig. DR1).

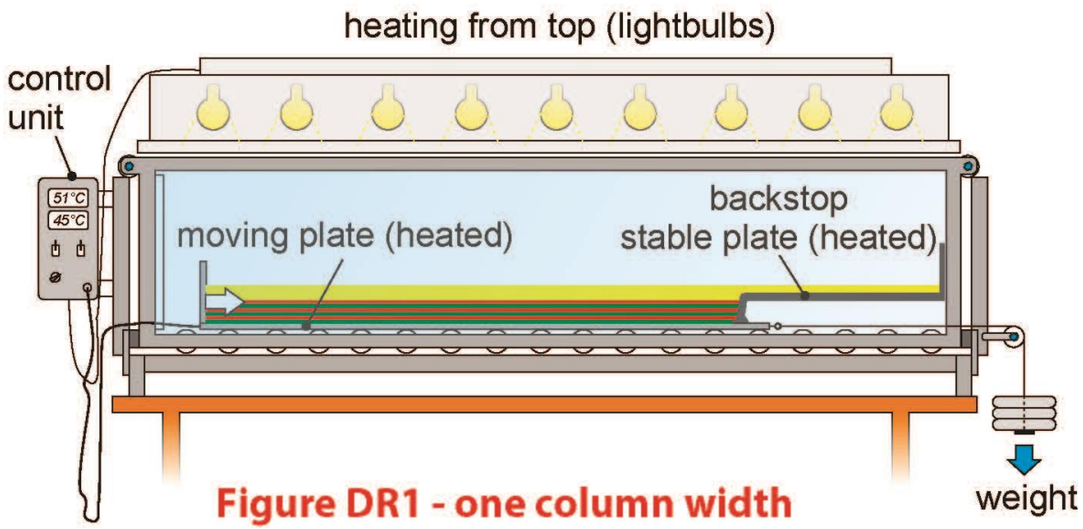

Figure DR1. Scheme of the analogue modelling apparatus used for modelling of the crustal-scale detachment folds. Long (movable) plate is one m-long. Both, the moving plate and the backstop can be heated homogenously along their entire length at a temperature adjusted at the control unit. Heating from the top prevented heat loss from the model and maintained a stable temperature gradient across the model.

During the experiment, the long plate (pro-wedge part of the orogen) is moved against the backstop of the stable plate (retro-wedge) by a force of a weight attached to the steel rope pulling the long plate (Fig. DR1). A vertical wall (10 cm high) terminates the long plate and is aimed at supporting the superposed layers that are being deformed by shortening of the multilayer against the backstop. The backstop consists of two segments – a ramp and a plateau. The angle of the ramp and the plateau is adjustable. For the experiment described below, a 4 cm high ramp was inclined at 65° towards the long plate and the plateau was horizontal. Insulating plates (polystyrene) cover the glass panes in order to prevent heat loss before the experimental run.

Analogue materials and experimental preparation

For upper brittle crust, we have used fine-grained, pure quartz sand (grain size 0.017 mm), typically used in crustal-scale physical models (e.g. Sokoutis et al., 2005). The sand is characterized by a density of 1460 $kg.m^{-3}$, a static friction angle of 32.47° and cohesion of 95.36 Pa. Partially molten middle to lower crust was simulated by a commercial macrocrystalline paraffin wax with a density of 810 $kg.m^{-3}$ and a melting temperature of 52°C (Paramo 50-52, manufactured in Czech Republic).

The viscosity of the wax was measured using the VT550 Haake viscometer with coaxial cylinders (MV 1 cylinder) in a temperature range of 44°C to 52°C. The wax is characterized by Newtonian rheology from 46°C to 52°C and dynamic viscosity ranging from 2.03 mPa.s at 46°C to 0.46 mPa.s at 52°C (Table DR2). At lower temperatures (<44°C), the wax solidified, and viscosity measurements were beyond the technical limits of the instrument used. Therefore, for temperatures of the paraffin around 34-44°C, we consider effective viscosities measured by Rossetti et al. (1999) using the uniaxial compression tests on a similar paraffin wax at the same homologous temperatures (T/Tm, where Tm is the melting point; see Table DR2). Commercial paraffin measured by Rossetti et al. (1999) displayed only a 2°C higher melting point than our wax, and non-Newtonian rheology of solid paraffin at lower temperatures ($T/T_m < 0.7$) that ranged between 10^5 to 10^8 Pa.s (Table DR2).

TABLE DR2. DYNAMIC VISCOSITIES OF THE WAX MEASURED AT TEMPERATURES THAT CHARACTERIZE THE VISCOSITY GRADIENT OF THE PARAFFIN WAX IN THE EXPERIMENT

Temperature (°C)	34	38	44	46	48	50	52
Viscosity (mPa.s)	*10^8 Pa.s*	*10^5Pa.s*	6.84	2.03	0.85	0.53	0.46

Note: Values for viscosities of 105-8 Pa.s are adopted from Rossetti et al. (1999) and are linked to the same homologous temperatures of the paraffin wax used in this study. Note that the first two values are indicated in Pa.s.

Before the experimental run, a stack of 6 colored wax layers (each 0.5 cm-thick) was placed on the movable heating plate. Sidewalls of the wax multilayer were sprayed with a silicon oil to provide a free-slip surface along the vertical glass panes. In the next stage, the wax multilayer was pre-heated from bottom to top to make sure it is soft and gained enough heat. A horizontal layer of warm sand was then superposed on the moving plate (3 cm-thick) and the stable plate (2 cm-thick) in order to avoid cooling down of the wax. One marker of dark sand was included in the sand layer. The multilayer was then heated to adjust a constant temperature gradient in the column; 52 °C at the base and 45 °C

at the top of the sand layer. The stable plate was pre-heated at a moderate temperature of 45 °C to prevent cooling of the wax at the backstop interface.

In our approach, we attempted to mimic the temperature-dependent viscosity variation with depth in the ductile layer using the heated paraffin wax. Accordingly, the rheological profile from the bottom of the wax layer to the interface with the overlying sand can be divided into three sub-layers: i) completely molten wax with Newtonian rheology and low viscosity of 0.46 mPa.s (Table DR2), ii) mushy, partly crystallized, but still molten wax (6.84 mPa.s at 44°C), and iii) non-Newtonian viscosity of plastic wax in temperature range of 34–44°C defining the stiffest layer in the wax multilayer. Since for this latter stiffest layer, the viscosity could not have been measured using the coaxial cylinder viscometer, we consider viscosity values of a similar paraffin wax measured by Rossetti et al. (1999) at the same homologous temperatures that ranged between 10^5 to 10^8 Pa.s (Table DR2).

For the purpose of the scaling analysis of the experiment with respect to nature, we considered the viscosities of the partly crystallized mushy wax at 44°C with viscosity of 6.84 mPa.s measured by the coaxial cylinder viscometer (Table DR2). This mushy wax in our experiment reflects the migmatitic interlayer between the brittle superstructure of the Chandman dome and the molten to partially molten lower crustal infrastructure. For evaluation of the impact of the gravitational forces on the folding dynamics (using equation 18 of Duretz et al. 2011, see Appendix C), we consider the viscosity of the stiffest layer in the entire multilayer of 10^5 Pa.s (solid, but pseudoplastic paraffin wax at $T/T_m \sim 0.7$-0.8; Rossetti et al., 1999).

Scaling relationships

The model was scaled according to the principles of geometric and dynamic-rheological similarity (Hubbert, 1937; Weijermars and Schmeling, 1986; Sokoutis et al., 2005). The geometric similarity is constrained by the scaling ratio $l^* = 2 \times 10^{-6}$ with respect to the 30 km original crustal thickness of the Chandman dome. The accuracy of the dynamic scaling was tested by calculating the non-dimensional numbers given by ratios between the forces acting on the models (Ramberg, 1981). We calculated the ratio between the gravitational and viscous stresses (Ramberg number, R_m; Weijermars and Schmeling, 1986; Sokoutis et al., 2005):

$$R_m = \frac{gravitational\ stress}{viscous\ stress} = \frac{\rho_d g h_d}{\eta \dot{\varepsilon}} = \frac{\rho_d g h_d^2}{\eta V}$$

where ρ_d and h_d are the density and thickness of the ductile layer (paraffin wax), respectively, g is the gravity acceleration (g = 9.81 m.s^{-2}), η is the viscosity of the ductile layer and $\dot{\varepsilon}$ is the strain rate given by the ratio between the mean velocity of convergence V and the thickness of the ductile layer h_d. Scaling of the brittle deformation was achieved by calculating the ratio between the gravitational stress and cohesive strength (R_s; Ramberg, 1981; Sokoutis et al., 2005):

$$R_S = \frac{gravitational\ stress}{cohesive\ strength} = \frac{\rho_b g h_b}{\tau_c}$$

where ρ_b and h_b are the density and thickness of the brittle layer, respectively, g is the gravity acceleration and τ_c the cohesive strength of the brittle layer. For a correctly, dynamically scaled model, the R_m and R_s calculated for both, the model and the original (Chandman dome), respectively, should be similar (Table DR3), within the same order of magnitude.

TABLE DR3. SCALING PARAMETERS FOR BRITTLE AND DUCTILE DEFORMATION OF THE EXPERIMENT. SYMBOLS ARE DEFINED IN THE TEXT

	Upper crust (sand in the experiment)			Lower crust (wax in the experiment)						
	ρ_b (kg.m^{-3})	h_b (m)	τ_c (Pa)	ρ_d (kg.m^{-3})	h_d (m)	η (Pa.s)	g (m.s^{-2})	V (m.s^{-1})	R_m	R_s
Model	1460	0.03	95	810	0.03	6.8×10^{-3}	9.81	8×10^{-5}	13069243	5
Nature	2650	1.5×10^{4}	6×10^{7}	2750	1.5×10^{4}	1×10^{14}	9.81	6.3×10^{-10}	95710775	6

Note: The viscosity of the ductile layer in the experiment corresponds to the wax paraffin viscosity measured at 44°C (Table DR2)

The scaling analysis (Table DR3) compares the viscosities (η) of the partially crystallized wax measured at 44°C (6.84 mPa.s, Table DR2) and a migmatite, for which the viscosity

is indirectly estimated from the viscosity of a suspension of a hydrous granite (hydrous rhyolitic melt containing ~2 wt.%, Giordano et al., 2008) of ~10^7 Pa.s and 60-80 vol.% of crystals that increases the effective viscosity of the crystal-free melt 6-7 orders of magnitude to maximum ~10^{14} Pa.s (Costa et al., 2009). This scaling analysis (Table DR3) shows comparable values of both the R_m and R_s of the experiment and natural original, respectively. Alternatively, for the dynamic scaling analysis of the ductile layer, we can consider the viscosity of the completely molten wax (0.46 mPa.s at 52°C) as an equivalent to the granite melt of ~10^8 Pa.s (containing 1.5 wt.% water, corresponding to the 5.15 mol.% water of migmatite sample M109P72 of Broussolle et al., 2015) with 40-50 vol.% crystals that will render effective viscosity of the melt+crystal suspension of ~10^{13} Pa.s (Giordano et al., 2004, 2008; Costa et al., 2009). Calculating the R_m with the latter values for the experiment and original (nature, Chandman dome), will give again values within the same order of magnitude.

In summary, we can suggest that the rheological stratification of the sand and the wax fairly well mimics the rheological stratification before the folding of the Chandman dome. The partially molten wax implements a viscosity gradient from the completely molten layer at the bottom of the lower crust to a partially molten layer close to the interface between the weak lower crust and brittle upper crust. The scaling analysis also shows that the rheological properties, dimensions and timescales are within reasonable ranges to consider the experiment in terms of close dynamic similarity with the folding of the Chandman dome.

APPENDIX C: CALCULATION OF DIAPIRIC VELOCITY AND BACKGROUND VELOCITY

In order to constrain potential contribution of the diapiric forces to the formation of the detachment fold in the analogue model, we use equation 18 of Duretz et al. (2011). The vertical velocity linked to formation of a Rayleigh-Taylor instability (V_{RT}) is expressed against the density ratio between the layers ($\delta\rho$), the gravity (g), the height of the initial perturbation of the interface (A), the thickness of the crust (H_{crust}), the viscosity of the stiffest layer (η_{MC}) and the background strain rate ($\dot{e}_{BG}$).

$$V_{RT} \propto \frac{\delta \rho g H_{crust}}{\eta_{MC}} \times A \times \dot{e}_{BG}$$

The viscosity of the stiffest layer (η_{MC}) is 10^5 Pa.s (following measurements of Rosettti et al. 1999, see Appendix B), the initial perturbation of the interface A is chosen at 0.003 m, corresponding to 10% of the total wax thickness, background strain-rate is $((L_t\text{-}L_0)/L_0)/dt = ((0.6\text{-}0.96)/0.96)/4500 = -8.333305 \times 10^{-5}\ s^{-1}$.

The background velocity is defined as total shortening of the box divided by total time of experiment.

According to these calculations, the rate of box shortening is ~30 million time faster than diapiric rate.

APPENDIX D: ANALYTICAL SOLUTION DESCRIBING GEOMETRICAL EVOLUTION OF THE DETACHMENT FOLD

Knowing H, h, C_h, LZW and θ, the initial length of limbs (L_0) and fold crest width (C) can be written as follows (see figure 13 for explanation of the different symbols):

$$L_0 = LZW / sin(\theta)$$

$$C = C_h + 2 \times (H\text{-}h)/tan(\theta)$$

Note that the initial width of the detachment fold is given as $W_0 = C + 2 \times L_0$.

With increasing displacement D, the area/volume of fold core (A) is a function of fold amplitude (a), inner fold crest width (C_h), length of fold limb (L_D) and its angle (α):

$$L_D = LZW / \sin(\pi - \theta - \alpha)$$

$$a = L_D \times sin(\alpha)$$

$$i = L_D \times cos(\alpha)$$

$$A = a \times (i + Ch)$$

The corresponding displacement is $D = 2 \times (L_0 - i)$.

Assuming that there is not volume change within the folded layer, the evolution of area/volume of the fold core A in respect to either the limb angle (α) or displacement (shortening %) is not balanced with the displaced layer area/volume $S = D * h$. The actual difference between A and S reflects the potential to mass transfer into or out of the fold core. See text for details.

REFERENCES CITED

Broussolle, A., Štípská, P., Lehmann, J., Schulmann, K., Hacker, B. R., Holder, R., Kylander-Clark, A. R. C., Hanžl, P., Racek, M., Hasalová, P., Lexa, O., Hrdličková, K., and Buriánek, D., 2015, P–T–t–D record of crustal-scale horizontal flow and magma-assisted doming in the SW Mongolian Altai: Journal of Metamorphic Geology, v. 33, no. 4, p. 359–383, doi:10.1111/jmg.12124.

Costa, A., Caricchi, L., and Bagdassarov, N., 2009, A model for the rheology of particle-bearing suspensions and partially molten rocks: Geochemistry, Geophysics, Geosystems, v. 10, no. 3, doi:10.1029/2008GC002138.

Dingwell, D.B., Hess, K.U., and Romano, C., 1998, Viscosity data for hydrous peraluminous granitic melts: Comparison with a metaluminous model: American Mineralogist, v. 83, no. 3-4, p. 236–239, doi:10.2138/am-1998-3-406.

Duretz, T., Kaus, B. J. P., Schulmann, K., Gapais, D., and Kermarrec, J. J., 2011, Indentation as an extrusion mechanism of lower crustal rocks: Insight from analogue and numerical modelling, application to the Eastern Bohemian Massif: Lithos, v. 124, no. 1–2, p. 158–168, doi:10.1016/j.lithos.2010.10.013.

Giordano, D., Romano, C., Papale, P., and Dingwell, D. B., 2004, The viscosity of trachytes, and comparison with basalts, phonolites, and rhyolites: Chemical Geology, v. 213, no. 1–3, p. 49–61, doi:10.1016/j.chemgeo.2004.08.032

Giordano, D., Russell, J.K., and Dingwell, D.B., 2008, Viscosity of magmatic liquids: A model: Earth and Planetary Science Letters, v. 271, no. 1-4, p. 123–134, doi:10.1016/j.epsl.2008.03.038.

Hubbert, M. K., 1937, Theory of scale models as applied to the study of geologic structures: Geological Society of America Bulletin, v. 48, no. 10, p. 1459–1519, doi:10.1130/gsab-48-1459.

Jourdan, F., Verati, C., and Féraud, G., 2006, Intercalibration of the Hb3gr $^{40}Ar/^{39}Ar$ dating standard: Chemical Geology, v. 231, no. 3, p. 177–189, doi:10.1016/j.chemgeo.2006.01.027.

Ramberg, H., 1981, Gravity, deformation and the Earth's crust: 2nd Edition, New York, Academic Press.

Renne, P. R., Mundil, R., Balco, G., Min, K., and Ludwig, K. R., 2010, Joint determination of 40K decay constants and 40Ar∗/40K for the Fish Canyon sanidine standard, and improved accuracy for $^{40}Ar/^{39}Ar$ geochronology: Geochimica et Cosmochimica Acta, v. 74, no. 18, p. 5349–5367, doi:10.1016/j.gca.2010.06.017.

Rossetti, F., Ranalli, G., Faccenna, C., 1999. Rheological properties of paraffine as an analogue material for viscous crustal deformation: Journal of Structural Geology v. 21, no. 4, p. 413–417, doi:10.1016/S0191-8141(99)00040-1.

Schoene, B., and Bowring, S., 2006, U–Pb systematics of the McClure Mountain syenite: thermochronological constraints on the age of the $^{40}Ar/^{39}Ar$ standard MMhb: Contributions to Mineralogy and Petrology, v. 151, no. 5, p. 615–630, doi:10.1007/s00410-006-0077-4.

Sokoutis, D., Burg, J.P., Bonini, M., Corti, G., and Cloetingh, S., 2005, Lithospheric-scale structures from the perspective of analogue continental collision: Tectonophysics, v. 406, no. 1-2, p. 1–15, doi:10.1016/j.tecto.2005.05.025.

Weijermars, R., and Schmeling, H., 1986, Scaling of Newtonian and non-Newtonian fluid dynamics without inertia for quantitative modelling of rock flow due to gravity (including the concept of rheological similarity): Physics of the Earth and Planetary Interiors, v. 43, no. 4, p. 316–330, doi:10.1016/0031-9201(86)90021-X.